



Insights into photocatalytic CO₂ reduction on C₃N₄: Strategy of simultaneous B, K co-doping and enhancement by N vacancies

Ke Wang^{a,c}, Jile Fu^b, Ying Zheng^{a,b,*}

^a Institute for Materials and Processes, School of Engineering, the University of Edinburgh, Edinburgh, EH9 3FB, UK

^b Department of Chemical and Biochemical Engineering, Western University, London, Ontario, N6A 5B9, Canada

^c Xi'an Modern Chemistry Research Institute, Xi'an, Shaanxi, 710065, China

ARTICLE INFO

Keywords:

C₃N₄ B, K co-doping

Nitrogen vacancies

Electronic structure modification

Photocatalytic CO₂ reduction mechanism

Enhanced basicity for CO₂ reduction

ABSTRACT

C₃N₄ is a promising non-metal photocatalyst for CO₂ conversion to value-added products, while it shows unsatisfactory performance due to the low CO₂ adsorption ability and poor utilization of the photo-excited charge carriers. The deficiency of electron donation sites and unoptimized electronic structure are the primary reasons behind. To address the challenges, herein, we propose a new synthesis strategy of rational co-doping of B, K elements in line with controllable introduction of N_v into C₃N₄ within one step during synthesis. The synergistic effects of the modification factors resulted in an enhanced C₃N₄ catalyst with an electron-rich surface and tailored electronic structure, which significantly facilitated the CO₂ adsorption and activation in sequence. Moreover, the drawback of single element doping is largely avoided due to the synergistic effects provided by this rational multiple modification strategy. A 5-h photocatalytic production of 5.93 μmol g⁻¹ CH₄ and 3.16 μmol g⁻¹ CO respectively were achieved using CO₂ and H₂O as feedstocks without the presence of any organic hole scavenger, which are 161% and 527% of CH₄ and CO produced by pristine C₃N₄.

1. Introduction

Since the graphite like C₃N₄ was reported as a semiconductor showing potential application in photocatalytic water splitting, it has attracted much attention from researchers working on developing low-cost and high-performance catalysts aiming on renewable fuel production [1,2]. Although tri-s-triazine (heptazine) based C₃N₄ as photocatalyst shows attractive properties such as good stability, low-cost and negligible toxicity, the pristine C₃N₄ fails to perform satisfactory catalytic activity comparing with other photocatalysts. Its weak performance is mainly attributed to the low efficiency in interlayer charge transfer, high recombination rate and unoptimized electronic structure [3,4].

To address the aforementioned challenges, heteroatom doping was developed to improve the catalytic performance by modifying the electronic structures of C₃N₄. Many elements such as B [5–7], O [8,9], P [10], S [11], Cl [12,13], K [14,15] etc. have been reported as dopants. The main improvements are summarized herein including optimisation of band edge positions, facilitation of carrier generation and transfer, suppression of carrier recombination and enhancement of adsorption of reactants [16,17]. Beyond single element doping discussed above, multi-element doping is a relatively new strategy in enhancing the

performance. S-P [18], Fe-P [19], O-Na [20], O-K [21], B-P [22], B-F [23], N-P-B [24], K-I [25], C-O [26] etc. co-doping systems have been reported to enhance the catalytic performance of C₃N₄. Ideally, the multiple dopants provide a comprehensive approach to overcome different intrinsic shortcomings of C₃N₄ simultaneously. Each of the dopants could play its role in modifying material structure or electronic structure properties. However, co-doping elements could also have similar energy-favourable doping sites and act duplicated functions. For example, when the doping elements that have large diameters, such as Na, K, P, F, Cl, Br and I etc., usually prefer to dope at the interstitial sites of C₃N₄ [13,16]. Doping elements such as S, P, F, Pt, Fe, Co, Ni etc. tend to generate the mid-gap dopant states that in turn could promote carrier recombination [11,13,23,27–30]. The substitutional dopants having smaller Mulliken electronegativity than C, N (eg. S, P, B,) are believed to upshift the conduction band minimum (CBM) while the substitutional dopants with larger Mulliken electronegativity (eg. F, Cl, O) behave the opposite [31–33]. Atoms contain more valence electrons than C and N (eg. O, S, P, Cl etc) will generate an electron donor state near the CBM. On the other hand, the dopants with less valence electrons will produce electron adaptor states near the valence band maximum (VBM) [34]. In the literature, neither the rationale of the choice of co-doped elements nor the interaction between the dopants have

* Corresponding author.

E-mail address: ying.zheng@uwo.ca (Y. Zheng).

<https://doi.org/10.1016/j.apcatb.2019.05.002>

Received 14 February 2019; Received in revised form 21 April 2019; Accepted 1 May 2019

Available online 03 May 2019

0926-3373/ © 2019 Elsevier B.V. All rights reserved.

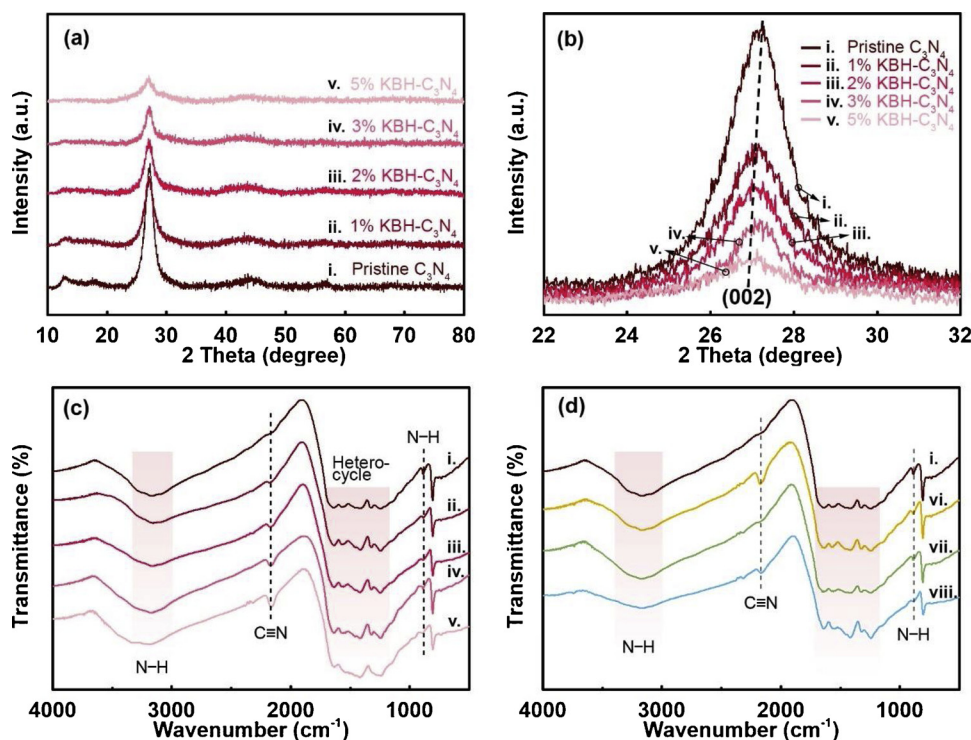


Fig. 1. (a) XRD patterns of KBH-C₃N₄ with different modification degrees and (b) magnification of the peaks attributed to (002) facet. The FTIR transmission spectra of (c) KBH-C₃N₄ with different modification degrees (i. pristine, ii. 1%, iii. 2%, iv. 3%, v. 5%) and (d) pristine-C₃N₄ (curve i.), 3% K-C₃N₄ (curve vi.), 3% B-C₃N₄ (curve vii.), 3% KB-C₃N₄ (curve viii.).

been clearly understood. The corresponding effects of different modification factors on catalytic performance need further elucidation. Besides heteroatom doping, the approach of vacancy introduction [14,35–38], creating atom vacancies in the lattice of C₃N₄, has been proven as an alternative effective way. The N vacancies (N_v) show high efficiency in narrowing bandgap and generating active sites compared to heteroatom doping. However, only appropriate amount of N_v can function positively [39–41]. N_v always generates an extra state in the middle of bandgap, which is deemed as the main recombination centre for the excited electron and holes in C₃N₄. Excessive N_v, especially the loss of N at the intersection of heptazine unit, could retard the electrical conductivity of C₃N₄. Thermal treatment of C₃N₄ under H₂ atmosphere is the most commonly used method to generate N_v [38,39]. However, it is an uncontrollable way for N_v introduction due to the usage of excessive H₂.

Photocatalytic CO₂ reduction with H₂O is an attractive application for C₃N₄ since it addresses greenhouse gas emission challenge and produce profitable fuel at the same time [42–44]. How to increase the photocatalytic CO₂ reduction performance of C₃N₄ and keep the catalysts free of transition metals are the main challenges. To be specific, an optimized C₃N₄ is expected to have the following features: (1) enhanced CO₂ adsorption and activation ability; (2) reduced bandgap for utilizing more light energy; (3) relatively high CBM as CO₂ reduction requires a high reduction potential to activate; (4) fast transfer of excited electrons on and across C₃N₄ layers; (5) the long lifetime of charge carriers. Modification of the molecular and electronic structure of C₃N₄ via doping and vacancy creation are proven to be very promising approaches [45]. For example, Sagara et al. [5] successfully prepared B-doped C₃N₄ that exhibited superior activities on CO₂ photoelectrochemical reduction. It was attributed to the enhanced water oxidation potentials achieved by the doping approach. Fu et al. [8] doped O into C₃N₄ so that light energy adsorption was promoted and carrier recombination was retarded. Since CO₂ is a Lewis acid, basic sites are preferred for the CO₂ adsorption [46]. Sun et al. [15,47] reported their etching method with KOH at high temperature to increase the catalytic performance of C₃N₄. The doped K along with more amino groups brought by etching were able to promote the activation of CO₂ over C₃N₄. Xia et al. [48] generated amine functional group via annealing

bulk C₃N₄ under NH₃ atmosphere to improve its capability of CO₂ adsorption and the CO₂ conversion was significantly increased.

In the present work, we developed a new strategy that integrates co-dopants K and B with controllable N_v. And the mechanism of enhanced photocatalytic CO₂ reduction performance was elucidated. Homogeneous distribution of K, B dopants and N_v with same molar concentration could only be achieved by using this one step strategy modifying by single-molecule compound: thermal polymerization of dicyandiamide (DCDA) with KBH₄. The advantage of this strategy relies on the synergistic effects and largely cancelled individual drawbacks of each modification factors. To be more specific, K is frequently doped at the interstitial site (also called vacancy site) to enhance CO₂ and C₃N₄ interlayer electron transfer; B, a substitutional dopant, helps to remain the high reduction potential for CO₂ by compensating the drawback of K. N_v narrows the bandgap and significantly enhances the CO₂ adsorption. The K and B co-dopants and N_v can act synergistically in promoting the photocatalytic CO₂ reduction on C₃N₄. Additionally, N_v with controllable quantity has been introduced by the self-limited generation of H₂ due to the decomposition of KBH₄. The modification strategy achieves 161% and 527% increases for CH₄ and CO respectively comparing with pristine C₃N₄. The achieved electron-rich catalyst surface and optimised electronic structure are proven to be attributed to the enhanced photocatalytic performance by both experimental and theoretical evidences. The CO₂ photocatalytic reduction pathway is further elucidated by in-situ diffuse reflectance infrared fourier-transform spectroscopy (DRIFTS).

2. Results and discussion

2.1. Photocatalyst characterization

2.1.1. Molecular structure characterization

X-ray diffraction (XRD) was used to characterize the crystal structure of our photocatalysts synthesized via thermal polymerization of DCDA with different amounts of KBH₄ powders. The effects of doping on the crystal lattice constants and interstitial doping between layers (as illustrated in Scheme S1 (d)) are expected to be verified by their XRD patterns. As shown in Fig. 1(a), all KBH-C₃N₄ with different

modification degrees present similar prominent peaks at around 27° . They are assigned to the (002) peaks of g- C_3N_4 derived from the stacking of layers interacting each other via van der Waals forces. The other smaller peaks centred at 13° represent in-plane repetition of heptazine units. Fig. 1(b) shows the magnified (002) peaks of all the prepared samples. A trend of slight shift towards lower angles can be observed. The increase of the layer distance could be possibly attributed to the layer distortion and K doping. While the latter is still under debate, K dopants have been claimed to have increased [16,17], decreased [14,49] or no effect [15] on the interlayer distance of C_3N_4 in the literature. It is also worth mentioning that the intensities of the peaks shown in the diffraction patterns drops with the higher modification degree. The gradual decrease in crystallinity suggests the distortions of C_3N_4 lattice brought by the N_v to the C_3N_4 .

Fourier-transform infrared (FTIR) spectra has been used to elucidate the evolution of molecular structure. As shown in Fig. 1(c), the strong bands ranging from 1200 to 1600 cm^{-1} are attributed to the heterocycles built up with C–N and C=N bonds [42]. The skeletal stretching model remains unchanged through the evolution, which confirms the molecular structure of heptazine unit has been well maintained. The peaks centred at 2177 cm^{-1} in curves ii, iii, iv, v are derived from the asymmetric vibration of the $C\equiv N$, the cyano groups. When the modification degree increases from 1% to 5%, the peak intensity grows correspondingly. On the contrary, at the same wavenumber, the curve i (pristine C_3N_4) shows no obvious peak. The peaks located at 887 cm^{-1} and the broad adsorption within the range from 3000 to 3700 cm^{-1} are brought by the N–H bonds [50]. Though insignificantly, the intensity reduction can still be seen from peak i to v. In order to differentiate the roles of different elements in modifying the structure of C_3N_4 , the FTIR spectra were acquired with the three controlling groups: K doped C_3N_4 (3% K- C_3N_4), B doped C_3N_4 (3% B- C_3N_4), and B, K co-doped C_3N_4 (3% KB- C_3N_4). The corresponding data are presented in Fig. 1(d). Compared with pristine C_3N_4 (curve i), only curve vi (3% K- C_3N_4) shows a sharp increase in the intensity of the peak centred at 2177 cm^{-1} , which is assigned to the $C\equiv N$ group. It leads to a conclusion that doping of K can facilitate the generation of the cyano group while B does not show the same function. It could be explained by the fact that potassium oxides react with the amine groups during the thermal polymerization process [14]. Increasing dosage of modification agent, KBH_4 , will result more in-situ H_2 generation, which in turn reacts with $-NH_x$ to form gaseous NH_3 so that more N_v was introduced. The phenomenon is supported by the fact that the $-NH_x$ peak intensity decreases with the rise of modification concentrations [39]. The nearly unchanged N–H peak intensities further confirmed that the in-situ H_2 treatment doesn't cause H doping to the molecular structure, which will be further verified by the organic elemental analyses in the following discussion (Table S2, in supporting information). The doping of H is less desirable since the H intends to saturate the N basic sites, which retards the CO_2 adsorption.

X-ray photoelectron spectroscopy (XPS) is a semi-quantitative tool to determine the site of the dopants by identifying their chemical environments. Fig. 2(a) shows the K2p spectra of the pristine and modified KBH- C_3N_4 . The pristine C_3N_4 shows no peak in the region and the peaks of $K2p_{1/2}$ and $2p_{3/2}$ are positioned at $295.7\text{--}295.5\text{ eV}$ and $293.0\text{--}292.8\text{ eV}$, respectively. The K2p peaks correspond to K–N bonds chemical environment, which are agreeable with the reported potassium azide [16,49]. The evidence strongly suggests that K dopants located at the interstitial sites between the layers. Peaks of K $2p_{1/2}$ and $2p_{3/2}$ exhibit a shift of 0.2 eV to lower energy when the concentration of KBH_4 increases from 1% to 5%. A similar shift is also observed in B1s profiles in Fig. 2(b). The B1s peaks are centred at the binding energy from 191.8 eV to 191.5 eV in modified C_3N_4 samples. It indicates the B–N bonds formed in the heptazine unit and B prefers to replace carbon at C1 position (bay position) in the heptazine structure (as illustrated in Scheme S1, supplementary information) [6,7]. C1s spectra are given in Fig. 2(c). The peaks positioned at $288.0\text{--}288.2\text{ eV}$ are assigned to C in

hetero-cycles, $N-C\equiv N$ [14,49]. A small binding-energy shift towards lower energy is also observed. The peaks at the binding energy of 284.8 eV are caused by the adventitious C (used as charging effects reference) [14]. The peaks corresponding to C– NH_x (286.4 eV) do not show an obvious increase, although more in-situ H_2 is generated when more KBH_4 is used. The N1s spectra shown in Fig. 3(d) could offer more information on molecular structure. In order to elucidate all the bonds formed with N, the dashed lines are plotted in the figure: peaks at 404.1 and 401.0 eV being associated with the NH_x groups, the peaks at 400.0 eV being attributed to the N3C (N bonding with 3 C atoms), the peaks at 398.7 eV referring to the N2C (N bonding with 2 C atoms), peaks at 398.0 eV to N–B bonds and peaks at 398.6 eV to the N–K bonds [14,49,51,52]. The changes in peak intensity suggests how the structure of C_3N_4 evolves during the modifications. The significant drop in the N2C intensity, shown in Fig. 2(d), confirms that H_2 is the source that induces N_v and the N2C is the most energy favourable one to lose. The peaks corresponding to the N–K and N–B groups rise, which further testifies the bond formation between dopants and C_3N_4 . The downshift of binding energies of B1s and N1s with increasing modification degree may be explained by the same reason: replacement of C by B (the less electronegative element) and the loss of N (the atom with the highest electronegativity) in the heptazine unit. It would largely increase the electron density for the remaining atoms in the doped system, which can enhance the screening effects of the core-level electrons. In addition, the concentrations of each atoms were also determined using XPS based on the C1s, N1s, B1s and K2p spectra peak areas with relative sensitivity factors [53]. As presented in Table S1, for all KBH- C_3N_4 with different concentrations, the C/N atomic ratios show small fluctuations and B/K atomic ratios are close to 1:1. It indicates the molar concentrations of B, K and N_v are nearly equal to each other in KBH- C_3N_4 .

The organic elemental analysis presents an additional quantitative analysis of the molecular structure evolution due to the modification. Table S2 shows the analysis results for KBH- C_3N_4 with different modification degrees and control groups including 3%K- C_3N_4 , 3%B- C_3N_4 and 3%KB- C_3N_4 . Comparing pristine C_3N_4 to the modified C_3N_4 samples, it can be seen that the C/N ratios remain similar, though only a small fluctuation could be observed. This result indicates that B is in favour of replacing C and in-situ generated H_2 causing the loss of N in the C_3N_4 structure. Moreover, it quantitatively proves that the B substituting C and N_v shows approximately 1:1 M ratio. The N loss due to in-situ H_2 treatment could also be confirmed by the higher C/N ratio of 3% KBH- C_3N_4 than 3%KB- C_3N_4 . A significantly lower C/N atomic ratio of 3%B- C_3N_4 demonstrates the main doping form of B is the substitution of C atoms inside the heptazine structure. K doping causes the loss of N but only slightly. The reason could be attributed to the formation of KOH during the synthesis process at ambient atmosphere and the KOH further reacts with C_3N_4 resulting the N_v [14,38]. Additionally, the H wt% shows small changes for all samples, which rules out the possible doping of H into the heptazine unit. All these quantitative results are in agreement with former FTIR and XPS analyses.

As a complementary method to XPS and organic elemental analyses in quantitative determination of doping degree, the thermogravimetric analysis (TGA) has been used and the results are presented in Fig. S1 and Table S3. The concentrations of K + B in KBH- C_3N_4 are very close to the values determined by XPS (Table. S1), which indicates the homogeneous distribution of the dopants both on the surface and in the bulk. It is in agreement with expectation, since the modification process happens during the synthesis process of C_3N_4 rather than a post-treatment. To further prove the homogeneous distribution of B, K dopants, an X-ray energy dispersive spectroscopy (EDS) elemental mapping was conducted with a scanning electron microscope (SEM) (Fig. S2). The corresponding EDS spectrum further confirms the existences of the C, N, B, K elements without other contaminants.

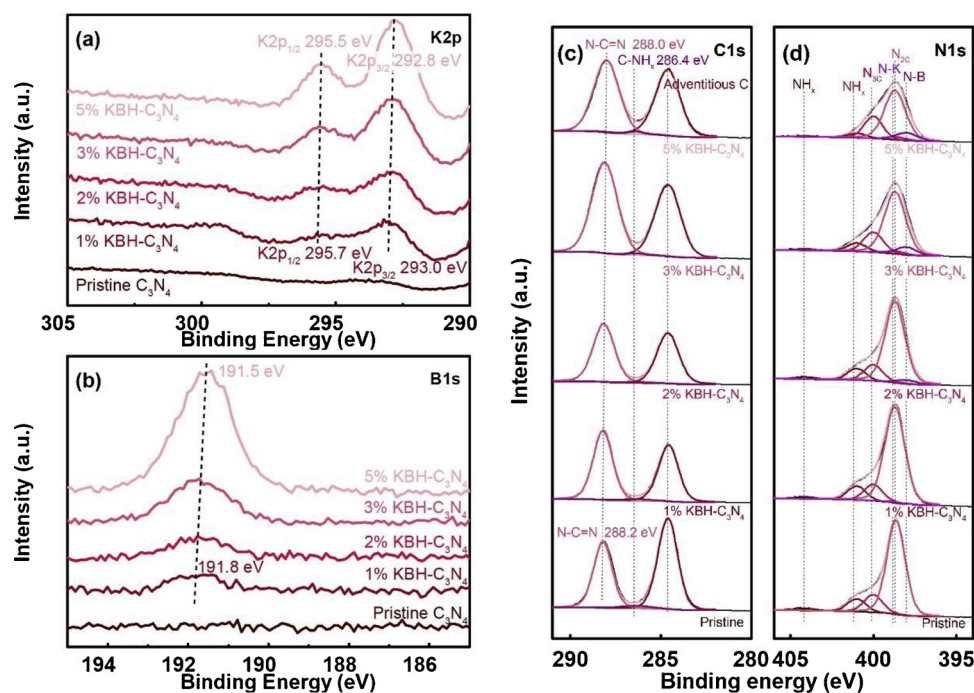


Fig. 2. XPS profiles of (a) K2p, (b) B1s, (c) C1s and (d) N1s spectra of pristine and KBH modified C₃N₄ (1%–5%).

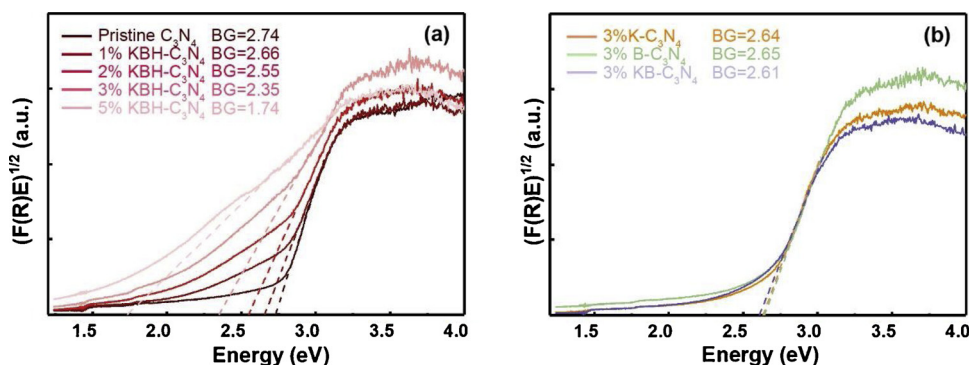


Fig. 3. Tauc plots for bandgap determination of (a) KBH-C₃N₄ with different modification degree (pristine, 1%, 2%, 3%, 5%) and (b) 3% K-C₃N₄, 3% B-C₃N₄ and 3% KB-C₃N₄.

2.1.2. Electronic structure characterization

The electronic structure including bandgap and band edge positions directly determines the light utilization ability, reduction/oxidation potential and excited carrier recombination rate of the photocatalysts. Therefore, it is more important to figure out how the KBH-modification changes the electronic structure of the C₃N₄ after identification of the molecular structure evolution. The band positions of prepared samples were determined via the combination of VBM positions calculated from the XPS valence band (VB) spectra and bandgap derived from the UV–vis diffuse reflectance spectroscopy (DRS) spectra.

The light absorption could be demonstrated via the UV–vis DRS spectra. The optical bandgaps of the samples could be derived from the Tauc plots and Kubelka-Munk theory, as shown in Fig. 3(a, b). The calculated optical bandgap energy for pristine C₃N₄ is 2.74 eV, which is very close to former reports [20,48]. And the bandgaps for KBH-C₃N₄ with 1–5% concentrations are determined to be 2.66, 2.55, 2.35 and 1.74 eV respectively. The monotonic narrowing of bandgap is due to the increasing modification degree. Comparing the optical bandgaps of control groups (Fig. 3(b)) with pristine C₃N₄ and 3% KBH-C₃N₄, the K, B co-doping could only narrow the bandgap by 0.13 eV while in-situ H₂ treatment decreases another 0.39 eV than K, B co-doping. The 3% K and 3% B-C₃N₄ has similar optical bandgap of 2.65 and 2.64 eV. The

corresponding UV–vis absorption curves are presented in Fig. S3(a, b) with Kubelka-Munk units. In summary, the N_v caused by in-situ H₂ treatment contributes the most to the bandgap narrowing.

The binding energy of the VBM for pristine C₃N₄ and 1%, 2%, 3%, 5% KBH-C₃N₄ is 2.18, 2.18, 2.13, 2.01 and 1.94 eV respectively, as shown in Fig. 4(a). The VBM positions show a slight decrease when KBH modification degree rises, while the discrepancies between each other are quite small (within 0.24 eV). In order to shed light on the role of individual modification factors, control groups of 3% K-C₃N₄, 3% B-C₃N₄ and 3% KB-C₃N₄ have been characterized at the same condition and the XPS VB spectra are presented in Fig. 4(b). It is exhibited that the K doping holds the capability to make the VBM more positive when doped into C₃N₄, which is in agreement with previously published reports [16,54]. On the contrary, B doping shows the opposite effects on VBM by shifting the VBM upwards, which agrees with the theoretic calculation and experimental results [23,55]. The N_v generated by H₂ treatments also bring the upshift to VBM, while the influence is not significant [39]. From determination of the VBM results, it clearly testifies the derivation of the synergistic effect between B and K. B dopants could compensate the detrimental effect of K doping, decrease of the reduction ability of CO₂, by upshifting the VBM.

In order to get a full understanding of the band alignments and

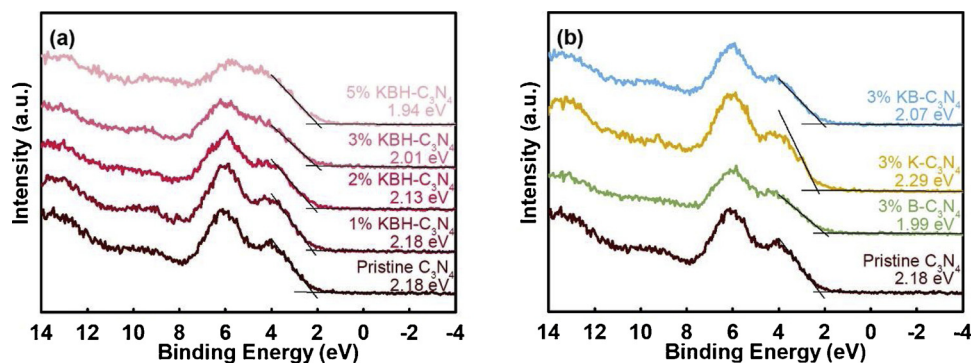


Fig. 4. XPS VB spectra of (a) pristine and KBH-C₃N₄ with different modification degree, and (b) control groups of 3% K-C₃N₄, 3% B-C₃N₄ and 3% KB-C₃N₄.

relative potentials towards different benchmark reactions, the VBM versus standard hydrogen electrode (SHE) could be calculated with following equation by estimating the work function Φ of the XPS analyser to be 4.37 eV and vacuum level of -4.44 eV (vs. SHE) [14,56,57]:

$$\text{VBM (vs. SHE)} = \Phi + E_{\text{binding}} - 4.44 \quad (1)$$

As the result, the VBM potentials (vs. SHE) of the pristine and 1%, 2%, 3%, 5% KBH-C₃N₄ are determined to be 1.62, 1.62, 1.57, 1.45 and 1.38 eV. Combining with the measured bandgap values, the band alignments of different samples could be calculated and the results are presented in Fig. 5 and the control group in Fig. S4.

The photoluminescence (PL) spectroscopy and time-resolved fluorescence spectroscopy are often used to evaluate the possibility of recombination and lifetime of the photo-excited carriers in photocatalysts. In Fig. S5(a), the fluorescence peak intensity of KBH-C₃N₄ show significant and continual decrease with rising modification degrees. This result supports the argument that the KBH-modification is able to limit the recombination of photo-excited electrons and holes in C₃N₄. Moreover, the extended lifetime of the charge carriers in modified KBH-C₃N₄ is further confirmed by conducting the time-resolved fluorescence spectroscopy characterized by monitoring the static PL peak wavelength. The fluorescence decay profiles and the corresponding exponential fittings were presented in Fig. S5(b, c). The average carrier lifetime of 3% KBH-C₃N₄ (Fig. S5(c)) is calculated to be 14.61 ns which is almost twice as long as the pristine C₃N₄ of 7.56 ns (Fig. S5(b)). The trapping effects of the dopants, N_v and the interlayer connection achieved by K dopants are supposed to be attributed to the longer carrier lifetime [4,16]. And atomic scale understandings including nearly no midgap state formed by K, B and non-coplanar existence of highest occupied molecular orbital (HOMO) and lowest unoccupied molecular orbital (LUMO) are proved by the electronic structure calculation, which is discussed in later section.

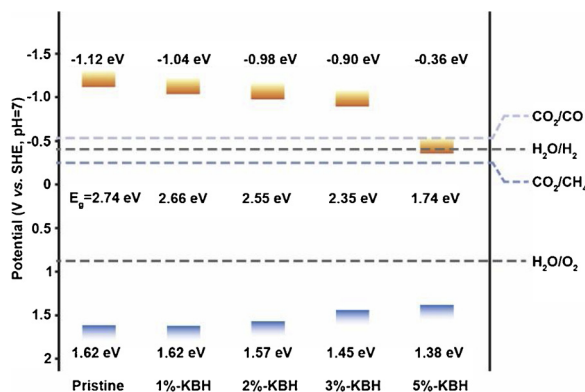


Fig. 5. Band alignment of the pristine and KBH-C₃N₄ with modification degrees of 1%, 2%, 3% and 5%.

2.1.3. Surface area characterization and CO₂ uptake capability

N₂ adsorption was conducted at 77 K to determine the specific surface area of prepared samples. The corresponding isotherms and calculated gravimetric surface areas based on multi-points BET (Brunauer, Emmett and Teller) theory are shown in Fig. S6 (a, b). The BET surface area for pristine C₃N₄ is 10.83 m² g⁻¹, which is quite similar to previous reports [58,59]. The 1%, 2%, 3%, 5% KBH-C₃N₄ exhibit the surface area of 8.46, 5.88, 5.32 and 4.47 m² g⁻¹ respectively, which clearly shows a decreasing trend. The BET surface area of control groups of 3% K-C₃N₄, 3% B-C₃N₄ and 3% KB-C₃N₄ are tested to be 7.26, 9.42, 7.45 m² g⁻¹ respectively. Based on these results, it is shown that the doping of B, K and N_v will cause the drop in specific surface area. The in-situ H₂ treatment causing N_v shows the strongest ability in reducing the surface area, which is believed due to its prominent capability in modifying the molecular structure. The high specific surface area does not always guarantee a high CO₂ conversion rate and CO₂ uptake ability is a more reliable criteria correlating directly with the CO₂ conversion performance [60]. The CO₂ temperature-programme desorption (CO₂-TPD) is a powerful tool to elucidate this important capability. Fig. 6(a) presents the CO₂-TPD profiles of KBH-C₃N₄ with different modification degrees. It is shown clearly that the pristine C₃N₄ has weak CO₂ adsorption ability with small desorption peak. The CO₂ uptake increases monotonically with the rise of modification degree with the peak at 3%-KBH C₃N₄. It drops afterwards to 5% KBH-C₃N₄. The desorption peak positions also shift to higher temperature for 3% KBH-C₃N₄. The significant increase on CO₂ adsorption and shift of desorption peak to higher temperature suggest that both the number and strength of basic sites of the photocatalyst prominently increase [60], which is due to the synergistic effects of K, B, N_v modifications. It is worth mentioning, the relatively low desorption temperature of CO₂ on pristine and KBH-C₃N₄ is ascribed to the weak Lewis basic sites that has also been observed in previous researches [6,61–64]. Being a Lewis acid, the CO₂ intend to be adsorbed on basic sites of catalysts and the electrons could transfer from the electron-rich sites on catalysts to the 2π* antibonding orbital of CO₂. The electron back-donation largely facilitates the activation and dissociation of CO₂ [15,47,65]. The K dopant has been proven as a kind of electron donors which could donate the electrons to the host and thus enhance the basicity of the catalysts. The role of N_v and B dopant in CO₂ adsorption and conversion have been less investigated than K [25]. Theoretically speaking, B is anticipated to increase the electron density of basic site (adjacent N) as it has less electronegativity than C and N. Moreover, the N_v will induce the electron abundance at the adjacent atoms [6]. Therefore, dopants B and K as well as N_v all play a positive role in promoting CO₂ adsorption. To differentiate their roles in modifying C₃N₄, control groups are carefully tested following the same CO₂-TPD procedure and the results are shown in Fig. 6(b). The experimental results confirm the CO₂ uptake enhancements caused by B, K dopant and N_v. Their promoting effects are in the order of N_v > B > K, which is in the same sequence as their ability of donating electrons. K in this study shows less prominent

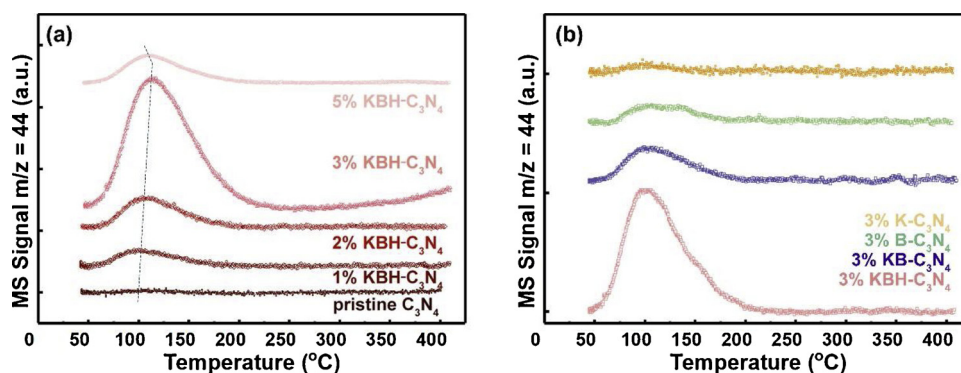


Fig. 6. The CO₂-TPD profiles of (a) pristine and KBH modified C₃N₄ and (b) control group of 3% K, B, KB modified C₃N₄.

effects than expected is due to its special interstitial doping sites in the layered C₃N₄ structure. In the conventional catalysts using transition metal oxides as supports, the alkali metal atoms stay on the surface of the catalysts, which will result in a direct contact with CO₂ and even forming alkali carbonates. However, K in multi-layer C₃N₄ dopes at the interstitial sites between layers without directly interaction with CO₂ on the surface. Its promotion effect is only the result of the electron donation. A fundamental understanding with the help of calculated charge density difference (CDD) plot and charge density analysis are presented in the next section. The last point needs to emphasize is the unexpected degradation in 5% KBH-C₃N₄. As presented in Fig. S7, the 5% KBH-C₃N₄ fails to show an increase in CO₂ uptake comparing with 5% KB-C₃N₄, while in 3% KBH-C₃N₄ the significant enhancement is unambiguous (Fig. 6(b)). It might be possibly explained by the following reason: N acts as basic sites in the heptazine unit for CO₂ adsorption [66] and the massive loss of N atoms will neutralize the benefits of the localized electron accumulation derived from N_v. Therefore, our synthesis strategy with controllable H₂ generation will prevent the over-generation of N_v and ensure an optimal performance. In summary, it could confirm the synergistic effects of K, B doping to C₃N₄ in enhancing the CO₂ adsorption and the N_v brought by the in-situ H₂ treatment contributes the most.

2.2. Theoretical calculations

First-principle calculation based on density functional theory (DFT) is used to help achieving the atom-scale understanding of modification. A 4-layer heptazine with energy favourable ABAB stacking has been used as the supercell to represent bulk C₃N₄ related structure. As discussed in the molecular structure section, K, B and N_v show molar ratios close to 1 in KBH-C₃N₄. Therefore, single K, B and N_v were introduced to the supercell to model the KBH-C₃N₄. Further details are presented in supporting information. The optimal doping sites for K, B and N_v have been figured out via calculating their formation energy (equations S-1 to S-6 in supporting information). The final optimized structure is presented in Fig. S8. The Heyd-Scuseria-Ernzerhof (HSE06) functional [67,68] has been reported to provide more accurate description of the defective C₃N₄ geometries by partially cancelling the self-interaction error [69,70]. It is adopted for the electronic structure calculation for C₃N₄ and KBH-C₃N₄ here. To elucidate the electronic structure, total and projected density of states (TDOS and PDOS) of pristine C₃N₄ and KBH-C₃N₄ have been plotted in Fig. 7(a, b). The contributions from the B s + p orbitals and K s + p orbitals are presented in Fig. S9 with the state population enlarged by 20 times. It demonstrates that K, B dopants do not significantly participate in forming the mid-gap states which are deemed as the recombination centre contributing to the carrier recombination [23]. The LUMO and HOMO of KBH-C₃N₄ are mainly constituted by N2p and C2p orbitals respectively, which is further elucidated in isosurface plot (Fig. 8(d)).

The CDD plots of KBH-C₃N₄ are presented here for illustrating

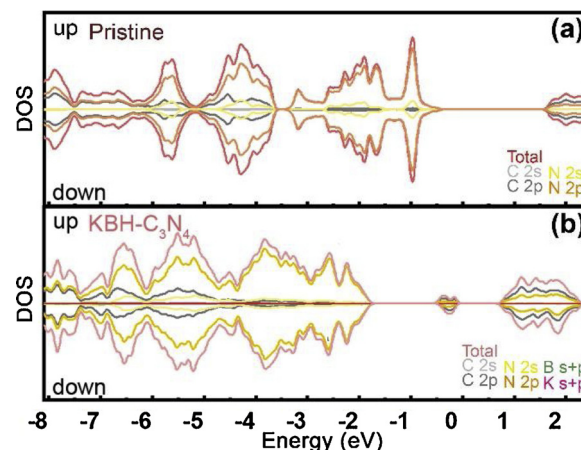


Fig. 7. Total and projected density of states (TDOS and PDOS) of (a) pristine C₃N₄ and (b) KBH-C₃N₄.

spatial electron density changes originated from KBH modification. The difference was calculated using the pristine C₃N₄ and K atom alone as the references [9,15,71,72]. As presented in Fig. 8(a–c), light pink and pale green represent accumulation and depletion of electrons respectively. The Fig. 8(b) shows a top view of CDD to gain an unambiguous view of the roles of N_v and B dopants. Both N_v and B will cause the electron-rich environment at their adjacent atoms. It is also worth mentioning the electron accumulation caused by N_v is stronger than B doping. This explains why N_v exhibits superior enhancement on CO₂ uptake than B doping. Fig. 8(c) presents the side view and places a clear illustration of the electronic role of K dopant. The existence of K will alternate the electron spatial distribution significantly, especially for the adjacent layers. The surface layer of the supercell is relatively less affected (Fig. 8(a)). When N atoms get close to K dopant, they exhibit an accumulation on the electron density, which agrees the formation of K–N chemical bonds as well as the electron donor role of K dopants. The electronic interaction between the K and adjacent layers could also make the electron transfer between layers possible. The calculation results further support our explanations on the emerging of K–N peaks in N 1s XPS spectrum and the corresponding shifts due to chemical environment changes. The AIM (atom in molecule) charge analyses (Bader analyses [73]) were calculated based on the charge density distribution and results of the surface layer is presented in Fig. S10(a, b). It is worth mentioning that the extra electrons caused by N_v are only partially localized at the adjacent C atoms, which is likely due to the π -conjugated electronic structure and covalent bonds in layered C₃N₄. The B dopant shows a Δq (electron transfer) of -2.10 which donates ~ 0.8 more electron than the C atom in the pristine C₃N₄. And N atoms as the Lewis basic sites showing Δq of 1.37, which gains ~ 0.3 more electron than the N at the same site in pristine C₃N₄. As the confirmation of the

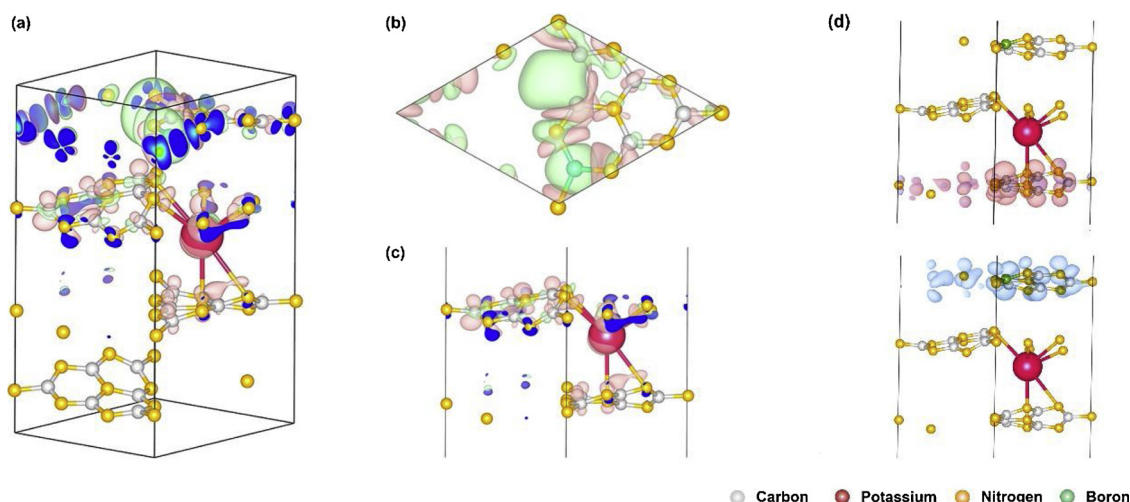


Fig. 8. (a) Full, (b) top and (c) side views of charge density difference (CDD) plots of optimized KBH-C₃N₄. The pale pink represents the accumulation of electrons and the pale green the electron depletion. (d) The HOMO and LUMO for the KBH-C₃N₄. The pale pink indicates the HOMO and navy blue the LUMO. The density isosurface is set to 0.015 and 0.005 e Bohr⁻³ for CDD plot and molecular orbital plot respectively (For interpretation of the references to colour in this figure legend, the reader is referred to the web version of this article).

electrons donating role, the K atom show a Δq of -1.55. Orbital plots could be used to understand the electron transfer under the excitation. It has been reported that in pristine g-C₃N₄, the HOMO and LUMO are quite localized and in coplanar relation, which is responsible for the high recombination rate [31]. Different from the pristine C₃N₄, the HOMO and LUMO in KBH-C₃N₄ are not adjacent but localized mainly at N and C atoms of different layers of C₃N₄, as shown in Fig. 8(d). It is in consistence with the PDOS plots (Fig. 7(b)). The non-coplanar spatial relationship between the HOMO and LUMO could significantly benefit the electron/hole separation and ensure a relative long carrier lifetime [74]. In summary, K acts to bridge the electron transfer between layers and B, N_v rearrange the electron and molecular orbitals spatial distributions. The multiple modifications all contribute to electron-rich sites and enhancement of the charge separation [75].

To rationalize the CO₂-TPD experimental results, the adsorption of CO₂ was calculated based on the slab models of both pristine C₃N₄ and KBH-C₃N₄. The optimal CO₂ adsorption site on pristine C₃N₄ has been comprehensively investigated in the literature [76] and CO₂ is adsorbed on N2 site of pristine C₃N₄, as shown in Fig. 9 (left side). The energy-favourable CO₂ adsorption site on KBH-C₃N₄ is found to be above the interstitial site and the optimized configuration is presented in Fig. 9 (right side). It has been reported that the CO₂ adsorption on pristine C₃N₄ is only slightly thermodynamically favourable [15,77] or even not spontaneous [78] based on the DFT calculations. Our CO₂ adsorption experiments also suggest a weak interaction between CO₂ and pristine C₃N₄ (Fig. 6(a)) [8,48]. The calculated CO₂ adsorption energy on the most energy favourable site of pristine C₃N₄ is only -0.093 eV. However, the CO₂ adsorption on optimal site of KBH-C₃N₄ is a much more spontaneous process with the adsorption energy of -0.361 eV, which is 4 times as much as the pristine one. The Bader charge analyses further elucidate that 0.23 e⁻ is transferred from the KBH-C₃N₄ surface to the CO₂, which is much more remarkable than the neglectable electron transfer from the pristine slab (0.02 e⁻). The accumulation of the electrons on the CO₂ will significantly enhance the activation and following conversion reactions.

2.3. Photocatalytic CO₂ reduction

Photocatalytic CO₂ reduction with H₂O was conducted over various modified samples under UV–vis irradiation generated by a 300 W Xenon Arc lamp in a batch reactor (illustrated in Scheme S3). Controlled experiment in dark generated zero detectable products

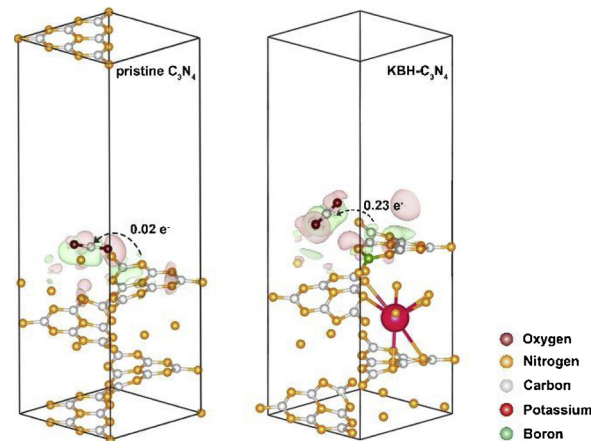


Fig. 9. Configurations of CO₂ adsorption on pristine (left) and KBH-C₃N₄ (right) after optimization. Charge difference distribution of the optimized CO₂ adsorption on KBH-C₃N₄ slab (pink colour indicating the electron accumulation, green the depletion. Isosurface: 0.0003 e Bohr⁻³). The number of electron transfer from adsorbent to CO₂ are based on grid-based Bader calculation results. (For interpretation of the references to colour in this figure legend, the reader is referred to the web version of this article).

converted from CO₂. The finding suggests that CO₂ can be converted only under light irradiation. The 5-h resulted products under UV–vis radiation over pristine C₃N₄ and 1%, 3% 5% KBH-C₃N₄, respectively, are presented in Fig. 10(a). As shown in the diagram, CH₄ and CO are the main products with pristine and KBH modified C₃N₄ as catalysts. None of CH₃OH, HCOOH or HCHO is detected in the head space. The pristine C₃N₄ shows a relatively low activity and only 3.69 and 0.6 μmol g⁻¹ were produced for CH₄ and CO, respectively. All KBH modified samples exhibit higher production rates than pristine C₃N₄. It is also worth noting that modification degree has an important effect on the catalyst performance. The 3% KBH-C₃N₄ is the best catalyst among the tested catalysts. It produces 5.93 and 3.16 μmol g⁻¹ CH₄ and CO respectively after 5 h, which are 1.61 and 5.27 times of pristine C₃N₄ respectively. The other two samples produce 4.4 μmol g⁻¹ CH₄, 1.25 μmol g⁻¹ CO (1% KBH-C₃N₄) and 4.42 μmol g⁻¹ CH₄, 1.08 μmol g⁻¹ CO (5% KBH-C₃N₄) respectively after 5 h. It is noted that more CH₄ was produced comparing with CO for all catalysts. This is due to the fact that CO requires a higher reduction potential than CH₄, which could be

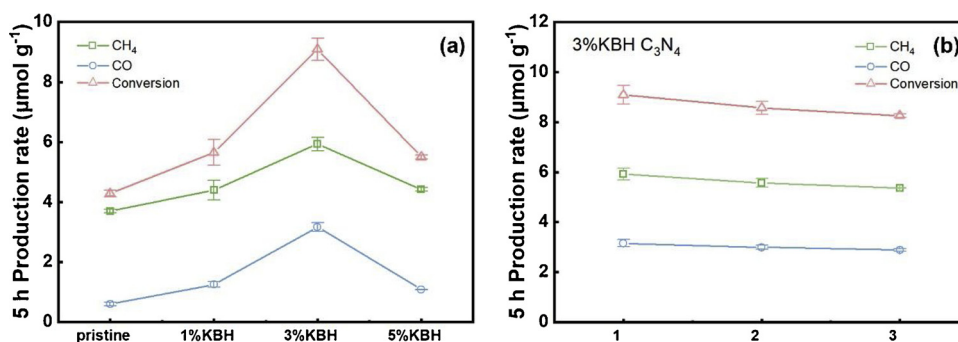
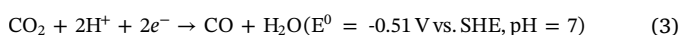
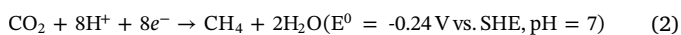


Fig. 10. (a) 5-h production of CO, CH₄ and total conversion of CO₂ on pristine C₃N₄, 1% KBH-C₃N₄, 3% KBH-C₃N₄ and 5% KBH-C₃N₄ using CO₂ and H₂O as feedstock under the irradiation of UV-vis light. (b) 5-h production of CO and CH₄ and total conversion of CO₂ in the stability tests of 3%KBH-C₃N₄ in 3 cycles.

described by the following equations (also illustrated in Fig. 5) [46]:



To further elucidate the correlation of different modification factors on catalytic performances, 3%K and 3%KB modified C₃N₄ were evaluated at the same reaction condition. As shown in Fig. S11, the 3% K-C₃N₄ produced 4.61 μmol g⁻¹ CH₄ after 5 h, while CO was not detected in the products. And 3% KB-C₃N₄ produces 0.93 μmol g⁻¹ CO and 5.53 μmol g⁻¹ CH₄. The better performance of 3% KB-C₃N₄ than 3% K-C₃N₄ could elucidate the role of B dopant in KBH-C₃N₄: facilitating the CO₂ activation. Since the CO production requires higher reduction potential as indicated by (Eqs. (2) and (3)), the higher CBM achieved by B dopants could compensate the side effects of K dopant and reach a better CO₂ conversion. The further improvement of both the CO and CH₄ production over 3% KBH-C₃N₄ than 3% KB-C₃N₄ testifies the enhancement brought by N_v.

To verify the stability of the catalysts, the 3%KBH-C₃N₄ was tested at the identical condition for 3 cycles and the CO and CH₄ production results are presented in Fig. 10(b). After 15 h of reaction, the photocatalysts show only insignificant degradation in terms of the 5-h production, which only drops 9.3% and 8.5% in CH₄ and CO respectively. The experimental results exhibit a good stability for the 3%KBH-C₃N₄ in the CO₂ photocatalytic conversion reaction. To figure out the reason of catalytic performance decrease after 15 h reaction. The powder after 15-h reaction was extracted from the reactor and dehydrated at 80 °C, vacuum overnight. Then FTIR transmission spectra for fresh and recycled ones are compared in Fig. 11. As could be interpreted in Fig. 11, the peaks centred at 1622, 3423 and 3122 shows slightly increase in intensity. All these 3 peaks could be attributed to -NH groups [79,80]. It

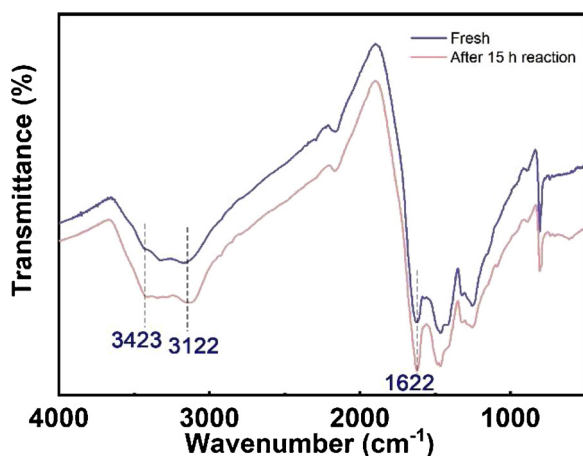


Fig. 11. The FTIR spectra of as-prepared fresh 3% KBH-C₃N₄ and after 15 h photocatalytic CO₂ reduction with water.

could be possibly due to the H chemisorbed on the N sites forming N-H bonds during the H₂O splitting. Considering the surface defects and dangling bonds on the surface of KBH-C₃N₄ are also the active sites, the H intends to saturate the dangling bonds and block the Lewis basic sites. Moreover, this specific chemical environment makes the combination of two adsorbed *H generating H₂ suffer from a high energy barrier. Therefore, the photocatalytic performances exhibit a slight decrease due to partial blocking of the active sites. The rise of H concentration has been found in defective C₃N_{4-x} prepared via H₂ treatment in the literature [38,81].

2.4. Mechanism investigation via in-situ DRIFTS

In-situ DRIFTS is used to elucidate the reaction intermediate species and reaction mechanism. The spectra recorded under both dark and UV-vis irradiation are presented in Fig. 12(a, b) for pristine C₃N₄ and 3%KBH-C₃N₄ respectively. To ensure the intensity of the peaks rationally comparable between these two spectra, the absorbances are normalized based on the peak intensity of gaseous CO₂ (2350 cm⁻¹). Thus, it rules out the influences of experimental setups. Before the reaction, all the sample surfaces were cleaned with flowing Ar at the temperature of 300 °C for 30 min. After cooling down to room temperature, CO₂/H₂O was introduced with Ar as the balance gas into the reactor, as illustrated in Scheme S4. CO₂ are generally adsorbed on the surface in the form of carbonate and bicarbonate with the presence of moisture. After exposing the CO₂/H₂O vapour to pristine C₃N₄ and KBH-C₃N₄ under dark for 20 min, the following species are observed on the surface: monodentate carbonate (m-CO₃²⁻, 1546–1547, 1464–1466) [82,83], bidentate carbonate (b-CO₃²⁻, 1701, 1688, 1352 cm⁻¹) [15,82–86], polydentate carbonate (p-CO₃²⁻, 1601 cm⁻¹) [87,88] and bicarbonate (HCO₃⁻, 1397, 1304 cm⁻¹) [83]. The 1650 cm⁻¹ peak is assigned to water adsorbed on the surface [15]. It is noted that all these carbonate peaks are much higher on the surface of 3% KBH-C₃N₄ than the pristine one. It is due to the fact that 3% KBH-C₃N₄ has stronger CO₂ adsorption ability than pristine C₃N₄, which is in agreement with the CO₂-TPD experiments and DFT calculation results discussed earlier. When reaching equilibrium in dark, UV-vis light was then irradiated on the catalysts with a power density of 40.3 mW cm⁻² using an optical liquid light guide coupled Xenon lamp. After irradiation for 60 min, new peaks centred at 1521, 1670 and 1755 cm⁻¹ emerged significantly, which are assigned to formate, CO₂⁻ and carbonyl species on both pristine and 3% KBH-C₃N₄ [48,82,89]. Along with the appearance of these new peaks, the CO₃²⁻ adsorption, centred at 1701, 1688, 1546–1547 cm⁻¹, significantly increase over both catalysts. The rise of carbonate adsorption peak under UV-vis irradiation suggests the carbonate species could be the primary reaction intermediates. More importantly, it is worth pointing out that the 3% KBH-C₃N₄ is capable to generate more anionic CO₂⁻ than the pristine C₃N₄ under UV-vis light irradiation. Being an intermediate species generated via direct CO₂ photocatalytic activation, CO₂⁻ is very active and tends

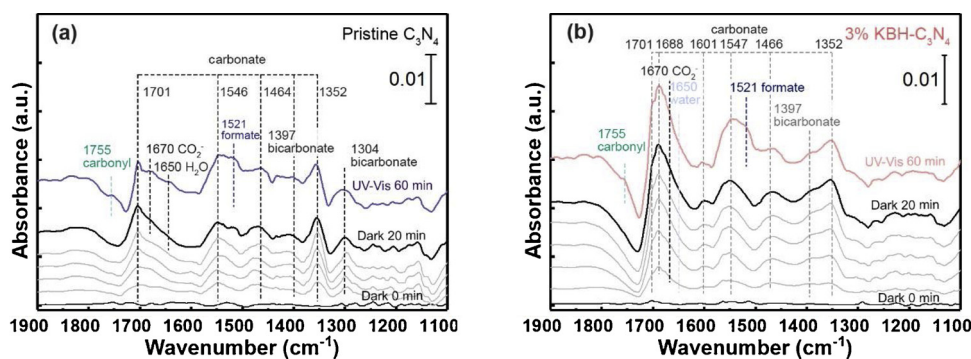


Fig. 12. DRIFT spectra of (a) pristine C_3N_4 and (b) 3% KBH- C_3N_4 with CO_2/H_2O under dark for 20 min and UV-vis irradiation for another 60 min.

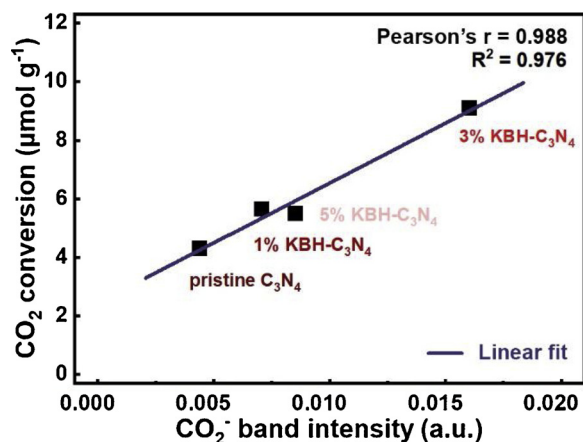


Fig. 13. Correlation between 5-h photocatalytic CO_2 conversion and the CO_2^- band increments in DRIFT spectra.

to react, via self-reaction or a proton-coupled electron, to CO , CO_3^{2-} and $HCOOH$. The generation of CO_2^- is usually believed as the rate determining step due to its high reduction potential required (-1.90 eV vs SHE) [46]. More importantly, electron-rich catalysts surface is usually indispensable for its generation [90]. A correlation between the concentration of CO_2^- and photocatalytic CO_2 conversion rate of TiO_2 was reported in the literature [90,91]. In our case, a positive correlation (correlation coefficient = 0.988) has been found between the CO_2^- band intensity increments of in-situ DRIFT spectra after 60 min UV-VIS irradiation and total CO_2 conversion after 5 h (Fig. 13). It suggests the CO_2^- is the key intermediate determining photocatalytic CO_2^- reduction rate on pristine and KBH- C_3N_4 . The DRIFT spectra of 1%-KBH and 5%-KBH C_3N_4 are presented in Fig. S12(a, b). It is worth emphasizing that the larger amount of CO_2^- generated on the surface of KBH- C_3N_4 should be attributed to the higher basicity of the surface. And the excess electron brought by N_v is believed to make the greatest contribution. Above discussion is also supported by the theoretical calculation results that the KBH- C_3N_4 contains electron-rich surface sites and more electron could transfer from KBH- C_3N_4 to CO_2 (Fig. 9). In summary, the major reaction intermediates observed in this work are CO_2^- , HCO_3^- , CO_3^{2-} and $HCOO^-$ (formate) on both pristine C_3N_4 and 3% KBH- C_3N_4 catalysts. A higher photocatalytic CO_2 conversion rate should be ascribed to the higher efficiency of CO_2^- species generation on 3% KBH- C_3N_4 than the pristine counterpart. To support the argument that formate as intermediate for CO and CH_4 production, additional control experiment of photocatalytic reduction of 5%v/v formic acid aqueous solution on the 3% KBH- C_3N_4 has been conducted in the absence of CO_2 atmosphere (details in SI). The chromatograph of the products after 30 min reaction is presented in Fig. S13. The main products of $HCOOH$ photocatalytic reduction with water are the CO_2 and H_2 , which is known in the dehydrogenation of formic acid process [92,93].

Meanwhile, the CO and CH_4 were also detected which could support the argument that formic acid/formate is the possible reaction intermediate for CO and CH_4 production. And the CO generated from formate decomposition could also act as the intermediate for CH_4 production via the carbene pathway (Eqs. 12–16) [94,95]. Finally, the possible mechanism of CO_2 photocatalytic conversion with H_2O on 3% KBH- C_3N_4 could be expressed by the following equations:



3. Conclusion

In this work, a new C_3N_4 optimization strategy combining doping and N_v has been developed. An electron-rich surface which remarkably enhances the CO_2 adsorption and activation has been achieved. In addition, K, B co-doping and N_v introduction in C_3N_4 could be reached by a facile one-step method. The specific role of each modification element has been carefully investigated and the synergistic effects are observed. K acts the electron donor and facilitates the electron transfers between the layers; N_v contributes the most to the CO_2 adsorption enhancement and basicity; B helps to maintain a high reduction potential and compensates the drawbacks of the K; N_v acts in lowering the CBM as well as in promoting CO_2 adsorption. The synergistic effects of multiple modifications synergistically achieve the 5 h production of $5.93 \mu mol g^{-1}$ CH_4 and $3.16 \mu mol g^{-1}$ CO respectively using pure CO_2 and H_2O without organic hole scavengers. It is 161% and 527% of the production over pristine C_3N_4 at the identical condition. The significantly improved CO_2 photocatalytic conversion performance of the catalysts approve the validity of the proposed new strategy of combination of doping and nitrogen vacancy introduction with a careful consideration

of the synergistic effects between the modification elements. More importantly, the selection of co-modification factors is rationalized. The prepared transition metal free KBH-C₃N₄ shows great performance as a candidate for photocatalytic solar fuel production and CO₂ control.

4. Experimental

4.1. Materials and preparation

All chemicals used in this work were analytical grade or equivalent without further purification. Dicyandiamide (DCDA), KBH₄, KNO₃ were purchased from the Acros Organics and B₂O₃ from the Sigma Aldrich. Ultrapure water (resistivity ≥ 18.2 M Ω) was used through our experiments. For synthesis of K, B co-doped C₃N₄ with nitrogen vacancy (N_v) due to in situ H₂ treatment (KBH-C₃N₄), 4 g DCDA was transferred into the agate mortar to mix with specific amounts of KBH₄ by 30 min grinding. The powder was then placed inside a ceramic crucible with lid. After annealing inside the muffle furnace at 550 °C for 2 h (ramping rate 2.3 °C min⁻¹), the KBH-C₃N₄ was successfully prepared. (Safety note: Although most of the H₂ generated by the thermal decomposition of KBH₄ will be consumed by the C₃N₄, it is still important to restrict the total amount of KBH₄ to safe level.) The syntheses of the control group samples, K doped C₃N₄ (3% K-C₃N₄), B doped C₃N₄ (3% B-C₃N₄), the process is the same except replacing the KBH with KNO₃ or B₂O₃. To verify the role of N_v, another control group B, K co-doped C₃N₄ without N_v (3% KB-C₃N₄) was synthesized via drying the DCDA and KBH₄ aqueous solution together at 100 °C to completely convert the KBH₄ to KBO₂ before thermal polymerization process.

4.2. Photocatalysts characterization

The crystal structure was characterized with an X-ray diffractometer (XRD, Bruker D2 Phaser). The surface chemical states and valence band maximum (VBM) positions of prepared samples were measured by the X-ray photoelectron spectrometer (XPS, ThermoFisher K-Alpha) with the monochromatic Al K α source. All XPS data have been calibrated referring to the C 1s peak (284.8 eV) derived from the adventitious carbon source to rule out the influence of surface charging [39]. The C, H, N elemental ratio measurements were conducted on an organic elemental analyser (Carlo Erba NA 2500). The optical absorption was measured with the diffuse reflectance spectroscopy (DRS) method on a UV-vis-NIR spectrometer (Shimadzu, UV-3600Plus) equipped with a praying mantis accessory (Harrick Scientific). The infra-red (IR) transmission spectra were measured on a Fourier transform infrared spectrometer (FTR, Shimadzu IRTracer-100) using a standard KBr pellet protocol with the DLATGS detector. Photoluminescence (PL) spectra was measured on a fluorescence spectrometer (RF6000, Shimadzu) with the excitation wavelength of 320 nm. The time-resolved fluorescence spectroscopy was conducted on the fluorescence spectrometer (FLS980, Edinburgh Instrument) with a pulsed excitation source and monitoring the fluorescence intensity decay at the corresponding PL peak wavelength. The samples were protected by the Ar inert atmosphere. The surface area was determined via the N₂ physical adsorption-desorption experiments at 77 K (Quantachrome, Autosorb-iQ). The CO₂ temperature-programmed desorption (TPD) were conducted on the same equipment with following procedures: 0.1 g samples are placed into a U-shape reactor and further treated under He flow (50 sccm) at 300 °C for 30 min. CO₂ was introduced and adsorbed on the samples for 45 min at room temperature. During the desorption process, the cell was heated to 400 °C with a ramping rate of 10 °C min⁻¹ under the flowing He (50 sccm). A mass spectrometer (MS, HAL 201, Hiden Analytical) is used to monitor the evolution of CO₂ by signalling $m/z = 44$. Scanning electron microscope (SEM, JEOL JSM-6390A) equipped with X-ray energy dispersive spectrometer (EDS, JEOL) was used to analyse the spatial distribution of K and B dopants.

4.3. In-situ DRIFTS measurement

In-situ diffuse reflectance infrared Fourier-transform spectroscopy (in-situ DRIFTS) was conducted using a commercial reactor (Praying Mantis HVC-DRP-5, Harrick) placed inside the infrared spectrometer (Shimadzu IRTracer-100) with a liquid nitrogen cooled MCT (Mercury Cadmium Telluride) detector (Scheme S4). A Xenon lamp (SLS400, Thorlab) coupled with a collimator and liquid light guide was used to provide the UV-vis light to drive the in-situ photocatalytic reaction. A KG-1 IR cut-off filter (Schott AG) is used to eliminate the thermal effects brought by the light source. The power of the light is measured via the pyroelectric optical power meter (PM16-401, Thorlab) and reaches ~ 40.3 mW cm⁻² on the surface of photocatalysts. Around 20 mg of sample are placed into the sample cup and the reaction temperature is fixed at 30 °C controlled by the chilled-water circulation and a PID controlled cartridge heater underneath the sample cup. The chamber was firstly purged with 20 sccm Ar flow and the samples were heated up to 300 °C with 30 min soaking time to get a clean surface. The baseline for the DRIFT spectra was recorded after the samples cooling down to 30 °C. The spectra for mechanism investigations were conducted using the following procedure: 5% CO₂/Ar was flowing through a water bubbler in the flow rate of 10 sccm for 20 min under darkness. Then the reactor valves are shut off to simulate the batch reaction for 60 min with UV-vis light. 116 scans with the resolution of 4 cm⁻¹ were averaged for one curve to ensure a high signal to noise ratio and the time interval of obtained curves was 1 min.

4.4. Catalytic evaluation

Photocatalytic performance on CO₂ reduction with water was evaluated with a stainless steel batch reactor with quartz window (diameter of 50 mm) under UV-vis light irradiation (as presented in Scheme S1 in supporting information). 0.1 g photocatalysts were loaded on borosilicate fibre filter (Fisher scientific) by vacuum filtration and drying at 100 °C in the oven. After loading the photocatalysts into reactor, the UV-vis light was irradiated on the photocatalysts under flowing Ar for 20 min to remove possible surface contamination. Then 0.8 mL water was added to the reactor and purged with CO₂ for 10 times before reaction. CO₂ is introduced in the reactor with the pressure of 2 bar after the last time of purge and the pressure is monitored by a digital compound gauge (DPGM8001-1V6, Omega engineering). A 300 W Xenon lamp (PE300, Excalitas Technologies) is used to mimic the solar light with UV-vis light output and ~ 430 mW cm⁻² light power density is achieved at the surface of the photocatalysts. All the reactions are conducted at the room temperature by forced air cooling the reactor with strong convection. The products were analysed with a gas chromatograph (GC-2010PLUS, Shimadzu) equipped with a TCD (thermal conductivity detector) and a FID (Flame ionisation detector) serially connected. A Shincarbon ST micropacked column (Restek Corporation) was used to separate the CO, CO₂, CH₄ from permanent gases.

4.5. Computational detail

First principle calculations based on DFT theory have been implemented with the Quantum Espresso package [96,97]. The PAW (projector-augmented wave) pseudopotentials [98–100] and plane-wave basis are used. The kinetic energy cut-offs for plane-wave basis sets and charge density and potential were 60 and 540 Ry respectively. The generalized gradient approximation (GGA) in form of the Perdew-Burke-Ernzerhof (PBE) [101] functional was used as the treatment of electron exchange and correlation for the geometry relaxation. Heyd-Scuseria-Ernzerhof (HSE06) hybrid functional [67,68] with 25% Hartree-Fock exchange was used in the electronic structure calculations based on the optimized structure. And long-range van der Waals (vdW) force was introduced to the system by using the Grimme-D3 dispersion correction for all calculations [102]. A gaussian smearing of 0.01 Ry

was exerted on the orbital occupation of all calculations. The self-consistency convergence threshold for each electronic step was 1×10^{-6} Ry. Geometry relaxations were conducted for all the structures until the force reached less than the criteria of 2×10^{-3} Ry Bohr⁻¹. A $1 \times 1 \times 4$ supercell of C₃N₄ with the repeated heptazine unit structure and 56 atoms in total was used to represent the pristine C₃N₄ before doping. B, K atoms were introduced into the supercell as substitutional or interstitial dopants for comparison. Slab models were built up by cleaving the (001) facet of optimized bulk structure and adding a vacuum layer of 15 Å to prevent the intervention. The bottom layer atoms were fixed and surface 3 layers were free to relax. The $4 \times 4 \times 4$ Monkhorst-Pack *k*-points grids were chosen to sample the Brillouin zone for bulk and $4 \times 4 \times 1$ mesh for slab models. All the plots related to the calculations were produced with the VESTA [103].

Acknowledgements

National EPSRC XPS Users' Service (NEXUS) located in the University of Newcastle, UK is appreciated for the help in XPS characterizations of the samples. This work has made use of the resources provided by the Edinburgh Compute and Data Facility (ECDF) (<http://www.ecdf.ed.ac.uk/>). The authors are also grateful for Prof. Neil Robertson and Dr. Gylan Odling in the School of Chemistry, the University of Edinburgh for the kind help of UV-VIS-NIR DRS measurements and discussions.

Appendix A. Supplementary data

Supplementary material related to this article can be found, in the online version, at doi:<https://doi.org/10.1016/j.apcatb.2019.05.002>.

References

- [1] X. Wang, K. Maeda, A. Thomas, K. Takanabe, G. Xin, J.M. Carlsson, K. Domen, M. Antonietti, A metal-free polymeric photocatalyst for hydrogen production from water under visible light, *Nat. Mater.* 8 (2009) 76–80.
- [2] W.J. Ong, L.L. Tan, Y.H. Ng, S.T. Yong, S.P. Chai, Graphitic carbon nitride (g-C₃N₄)-based photocatalysts for artificial photosynthesis and environmental remediation: are we a step closer to achieving sustainability? *Chem. Rev.* 116 (2016) 7159–7329.
- [3] X.C. Wang, S. Blechert, M. Antonietti, Polymeric graphitic carbon nitride for heterogeneous photocatalysis, *ACS Catal.* 2 (2012) 1596–1606.
- [4] S.W. Cao, H. Li, T. Tong, H.C. Chen, A.C. Yu, J.G. Yu, H.M. Chen, Single-atom engineering of directional charge transfer channels and active sites for photocatalytic hydrogen evolution, *Adv. Funct. Mater.* 28 (2018).
- [5] N. Sagara, S. Kamimura, T. Tsubota, T. Ohno, Photoelectrochemical CO₂ reduction by a p-type boron-doped g-C₃N₄ electrode under visible light, *Appl. Catal. B* 192 (2016) 193–198.
- [6] J.J. Zhu, T.T. Diao, W.Y. Wang, X.L. Xu, X.Y. Sun, S.A.C. Carabineiro, Z. Zhao, Boron doped graphitic carbon nitride with acid-base duality for cycloaddition of carbon dioxide to epoxide under solvent-free condition, *Appl. Catal. B* 219 (2017) 92–100.
- [7] Y. Wang, H.R. Li, J. Yao, X.C. Wang, M. Antonietti, Synthesis of boron doped polymeric carbon nitride solids and their use as metal-free catalysts for aliphatic C–H bond oxidation, *Chem. Sci.* 2 (2011) 446–450.
- [8] J. Fu, B. Zhu, C. Jiang, B. Cheng, W. You, J. Yu, Hierarchical porous O-Doped g-C₃N₄ with enhanced photocatalytic CO₂ reduction activity, *Small* 13 (2017) 1603938.
- [9] Z.F. Huang, J.J. Song, L. Pan, Z.M. Wang, X.Q. Zhang, J.J. Zou, W.B. Mi, X.W. Zhang, L. Wang, Carbon nitride with simultaneous porous network and O-doping for efficient solar-energy-driven hydrogen evolution, *Nano Energy* 12 (2015) 646–656.
- [10] Y.P. Zhu, T.Z. Ren, Z.Y. Yuan, Mesoporous phosphorus-doped g-C₃N₄ nanostructured flowers with superior photocatalytic hydrogen evolution performance, *ACS Appl. Mater. Interfaces* 7 (2015) 16850–16856.
- [11] K. Wang, Q. Li, B.S. Liu, B. Cheng, W.K. Ho, J.G. Yu, Sulfur-doped g-C₃N₄ with enhanced photocatalytic CO₂-reduction performance, *Appl. Catal. B* 176 (2015) 44–52.
- [12] C.Y. Liu, Y.H. Zhang, F. Dong, A.H. Reshak, L.Q. Ye, N. Pinna, C. Zeng, T.R. Zhang, H.W. Huang, Chlorine intercalation in graphitic carbon nitride for efficient photocatalysis, *Appl. Catal. B* 203 (2017) 465–474.
- [13] B.C. Zhu, J.F. Zhang, C.J. Jiang, B. Cheng, J.G. Yu, First principle investigation of halogen-doped monolayer g-C₃N₄ photocatalyst, *Appl. Catal. B* 207 (2017) 27–34.
- [14] H. Yu, R. Shi, Y. Zhao, T. Bian, Y. Zhao, C. Zhou, G.I.N. Waterhouse, L.Z. Wu, C.H. Tung, T. Zhang, Alkali-assisted synthesis of nitrogen deficient graphitic carbon nitride with tunable band structures for efficient visible-light-Driven hydrogen evolution, *Adv. Mater.* 29 (2017) 1605148.
- [15] Z.X. Sun, J.M.T.A. Fischer, Q. Li, J. Hu, Q.J. Tang, H.Q. Wang, Z.B. Wu, M. Hankel, D.J. Searles, L.Z. Wang, Enhanced CO₂ photocatalytic reduction on alkali-decorated graphitic carbon nitride, *Appl. Catal. B* 216 (2017) 146–155.
- [16] T. Xiong, W.L. Cen, Y.X. Zhang, F. Dong, Bridging the g-C₃N₄ interlayers for enhanced photocatalysis, *ACS Catal.* 6 (2016) 2462–2472.
- [17] W. Cui, J.Y. Li, W.L. Cen, Y.J. Sun, S.C. Lee, F. Dong, Steering the interlayer energy barrier and charge flow via biontentional transportation channels in g-C₃N₄: enhanced photocatalysis and reaction mechanism, *J. Catal.* 352 (2017) 351–360.
- [18] L.B. Jiang, X.Z. Yuan, G.M. Zeng, X.H. Chen, Z.B. Wu, J. Liang, J. Zhang, H. Wang, H. Wang, Phosphorus- and Sulfur-Codoped g-C₃N₄: Facile Preparation, Mechanism Insight, and Application as Efficient Photocatalyst for Tetracycline and Methyl Orange Degradation under Visible Light Irradiation, *ACS Sustainable Chem. Eng.* 5 (2017) 5831–5841.
- [19] S.Z. Hu, L. Ma, J.G. You, F.Y. Li, Z.P. Fan, G. Lu, D. Liu, J.Z. Gui, Enhanced visible light photocatalytic performance of g-C₃N₄ photocatalysts co-doped with iron and phosphorus, *Appl. Surf. Sci.* 311 (2014) 164–171.
- [20] W. Fang, J. Liu, L. Yu, Z. Jiang, W. Shangguang, Novel (Na, O) co-doped g-C₃N₄ with simultaneously enhanced absorption and narrowed bandgap for highly efficient hydrogen evolution, *Appl. Catal. B* 209 (2017) 631–636.
- [21] J.Y. Li, Z.Y. Zhang, W. Cui, H. Wang, W.L. Cen, G. Johnson, G.M. Jiang, S. Zhang, F. Dong, The spatially oriented charge flow and photocatalysis mechanism on internal van der Waals heterostructures enhanced g-C₃N₄, *ACS Catal.* 8 (2018) 8376–8385.
- [22] F. Raziq, Y. Qu, M. Humayun, A. Zada, H.T. Yu, L.Q. Jing, Synthesis of SnO₂/B-P codoped g-C₃N₄ nanocomposites as efficient cocatalyst-free visible-light photocatalysts for CO₂ conversion and pollutant degradation, *Appl. Catal. B* 201 (2017) 486–494.
- [23] K. Ding, L. Wen, M. Huang, Y. Zhang, Y. Lu, Z. Chen, How does the B,F-mono-doping and B/F-codoping affect the photocatalytic water-splitting performance of g-C₃N₄? *Phys. Chem. Chem. Phys.* 18 (2016) 19217–19226.
- [24] S. Zhao, J. Liu, C. Li, W. Ji, M. Yang, H. Huang, Y. Liu, Z. Kang, Tunable ternary (N, P, B)-doped porous nanocarbons and their catalytic properties for oxygen reduction reaction, *ACS Appl. Mater. Interfaces* 6 (2014) 22297–22304.
- [25] Y.R. Guo, Q. Liu, Z.H. Li, Z.G. Zhang, X.M. Fang, Enhanced photocatalytic hydrogen evolution performance of mesoporous graphitic carbon nitride co-doped with potassium and iodine, *Appl. Catal. B* 221 (2018) 362–370.
- [26] J.J. Wu, N. Li, X.H. Zhang, H.B. Fang, Y.Z. Zheng, X. Tao, Heteroatoms binary-doped hierarchical porous g-C₃N₄ nanobelts for remarkably enhanced visible-light-driven hydrogen evolution, *Appl. Catal. B* 226 (2018) 61–70.
- [27] G. Gao, Y. Jiao, E.R. Waclawik, A. Du, Single atom (Pd/Pt) supported on graphitic carbon nitride as an efficient photocatalyst for visible-light reduction of carbon dioxide, *J. Am. Chem. Soc.* 138 (2016) 6292–6297.
- [28] J.J. Liu, Effect of phosphorus doping on electronic structure and photocatalytic performance of g-C₃N₄: insights from hybrid density functional calculation, *J. Alloys. Compd.* 672 (2016) 271–276.
- [29] J.R. Ran, T.Y. Ma, G.P. Gao, X.W. Du, S.Z. Qiao, Porous P-doped graphitic carbon nitride nanosheets for synergistically enhanced visible-light photocatalytic H₂ production, *Energy Environ. Sci.* 8 (2015) 3708–3717.
- [30] Y. Zheng, Y. Jiao, Y. Zhu, Q. Cai, A. Vasileff, L.H. Li, Y. Han, Y. Chen, S.Z. Qiao, Molecule-level g-C₃N₄ coordinated transition metals as a new class of electrocatalysts for oxygen electrode reactions, *J. Am. Chem. Soc.* 139 (2017) 3336–3339.
- [31] X.G. Ma, Y.H. Lv, J. Xu, Y.F. Liu, R.Q. Zhang, Y.F. Zhu, A strategy of enhancing the photoactivity of g-C₃N₄ via doping of nonmetal elements: a first-principles study, *J. Phys. Chem. C* 116 (2012) 23485–23493.
- [32] Y. Xu, M.A.A. Schoonen, The absolute energy positions of conduction and valence bands of selected semiconducting minerals, *Am. Mineral.* 85 (2000) 543–556.
- [33] M.A. Butler, D.S. Ginley, Prediction of flatband potentials at semiconductor-electrolyte interfaces from atomic electronegativities, *J. Electrochem. Soc.* 125 (1978) 228–232.
- [34] G. Liu, L.Z. Wang, H.G. Yang, H.M. Cheng, G.Q. Lu, Titania-based photocatalysts—crystal growth, doping and heterostructuring, *J. Mater. Chem.* 20 (2010) 831–843.
- [35] P. Niu, G. Liu, H.M. Cheng, Nitrogen vacancy-promoted photocatalytic activity of graphitic carbon nitride, *J. Phys. Chem. C* 116 (2012) 11013–11018.
- [36] P. Yang, J. Zhao, W. Qiao, L. Li, Z. Zhu, Ammonia-induced robust photocatalytic hydrogen evolution of graphitic carbon nitride, *Nanoscale* 7 (2015) 18887–18890.
- [37] S.N. Li, G.H. Dong, R. Hailili, L.P. Yang, Y.X. Li, F. Wang, Y.B. Zeng, C.Y. Wang, Effective photocatalytic H₂O₂ production under visible light irradiation at g-C₃N₄ modulated by carbon vacancies, *Appl. Catal. B* 190 (2016) 26–35.
- [38] Q. Tay, P. Kanhere, C.F. Ng, S. Chen, S. Chakraborty, A.C.H. Huan, T.C. Sum, R. Ahuja, Z. Chen, Defect engineered g-C₃N₄ for efficient visible light photocatalytic hydrogen production, *Chem. Mater.* 27 (2015) 4930–4933.
- [39] P. Niu, L.C. Yin, Y.Q. Yang, G. Liu, H.M. Cheng, Increasing the visible light absorption of graphitic carbon nitride (melon) photocatalysts by homogeneous self-modification with nitrogen vacancies, *Adv. Mater.* 26 (2014) 8046–8052.
- [40] H.C. Lan, L.L. Li, X.Q. An, F. Liu, C.B. Chen, H.J. Liu, J.H. Qu, Microstructure of carbon nitride affecting synergistic photocatalytic activity: hydrogen bonds vs. Structural defects, *Appl. Catal. B* 204 (2017) 49–57.
- [41] V.W.H. Lau, V.W.Z. Yu, F. Ehrat, T. Botari, I. Moudrakovsky, T. Simon, V. Duppel, E. Medina, J.K. Stolarczyk, J. Feldmann, V. Blum, B.V. Lotsch, Urea-modified carbon nitrides: enhancing photocatalytic hydrogen evolution by rational defect engineering, *Adv. Energy Mater.* 7 (2017) 1602251.
- [42] W.J. Ong, L.K. Putri, Y.C. Tan, L.L. Tan, N. Li, Y.H. Ng, X.M. Wen, S.P. Chai, Unravelling charge carrier dynamics in protonated g-C₃N₄ interfaced with carbon

- nanodots as co-catalysts toward enhanced photocatalytic CO₂ reduction: a combined experimental and first-principles DFT study, *Nano Res.* 10 (2017) 1673–1696.
- [43] W.L. Li, Y.P. Hu, E. Rodriguez-Castellon, T.J. Bandosz, Alterations in the surface features of S-doped carbon and g-C₃N₄ photocatalysts in the presence of CO₂ and water upon visible light exposure, *J. Mater. Chem. A* 5 (2017).
- [44] L.Q. Ye, D. Wu, K.H. Chu, B. Wang, H.Q. Xie, H.Y. Yip, P.K. Wong, Phosphorylation of g-C₃N₄ for enhanced photocatalytic CO₂ reduction, *Chem. Eng. J.* 304 (2016) 376–383.
- [45] Y. Wang, F. Silveri, M.K. Bayazit, Q. Ruan, Y.M. Li, J.J. Xie, C.R.A. Catlow, J.W. Tang, Bandgap engineering of organic semiconductors for highly efficient photocatalytic water splitting, *Adv. Energy Mater.* 8 (2018).
- [46] X.X. Chang, T. Wang, J.L. Gong, CO₂ photo-reduction: insights into CO₂ activation and reaction on surfaces of photocatalysts, *Energy Environ. Sci.* 9 (2016) 2177–2196.
- [47] Z.X. Sun, S.C. Wang, Q. Li, M.Q. Lyu, T. Butburee, B. Luo, H.Q. Wang, J.M.T.A. Fischer, C. Zhang, Z.B. Wu, L.Z. Wang, Enriching CO₂ activation sites on graphitic carbon nitride with simultaneous introduction of electron-transfer promoters for superior photocatalytic CO₂-to-fuel conversion, *Adv. Sustain. Syst.* 1 (2017) 1700003.
- [48] P.F. Xia, B.C. Zhu, J.G. Yu, S.W. Cao, M. Jaroniec, Ultra-thin nanosheet assemblies of graphitic carbon nitride for enhanced photocatalytic CO₂ reduction, *J. Mater. Chem. A* 5 (2017) 3230–3238.
- [49] Y.X. Li, H. Xu, S.X. Ouyang, D. Lu, X. Wang, D.F. Wang, J.H. Ye, In situ surface alkalinized g-C₃N₄ toward enhancement of photocatalytic H₂ evolution under visible-light irradiation, *J. Mater. Chem. A* 4 (2016) 2943–2950.
- [50] S. Samanta, S. Martha, K. Parida, Facile synthesis of Au/g-C₃N₄ nanocomposites: an inorganic/organic hybrid plasmonic photocatalyst with enhanced hydrogen gas evolution under visible-light irradiation, *ChemCatChem* 6 (2014) 1453–1462.
- [51] P. Li, H.B. Li, X.L. Pan, K. Tie, T.T. Cui, M.Z. Ding, X.H. Bao, Catalytically active boron nitride in acetylene hydrochlorination, *ACS Catal.* 7 (2017) 8572–8577.
- [52] J. Sharma, T. Gora, J.D. Rimstidt, R. Staley, X-ray photoelectron spectra of the alkali azides, *Chem. Phys. Lett.* 15 (1972) 232–235.
- [53] K. Wang, C.J. Zhou, D. Xi, Z.Q. Shi, C. He, H.Y. Xia, G.W. Liu, G.J. Qiao, Component-controllable synthesis of Co(S₂Se_{1-x})₂ nanowires supported by carbon fiber paper as high-performance electrode for hydrogen evolution reaction, *Nano Energy* 18 (2015) 1–11.
- [54] S. Hu, F. Li, Z. Fan, F. Wang, Y. Zhao, Z. Lv, Band gap-tunable potassium doped graphitic carbon nitride with enhanced mineralization ability, *Dalton Trans.* 44 (2015) 1084–1092.
- [55] Q. Ruan, W. Luo, J. Xie, Y. Wang, X. Liu, Z. Bai, C.J. Carmalt, J. Tang, A nano-junction polymer photoelectrode for efficient charge transport and separation, *Angew. Chem. Int. Ed.* 56 (2017) 8221–8225.
- [56] S. Trasatti, The absolute electrode potential - an explanatory note (Recommendations 1986), *Pure Appl. Chem.* 58 (1986) 955–966.
- [57] Z.H. Hong, B. Shen, Y.L. Chen, B.Z. Lin, B.F. Gao, Enhancement of photocatalytic H₂ evolution over nitrogen-deficient graphitic carbon nitride, *J. Mater. Chem. A* 1 (2013) 11754–11761.
- [58] A.B. Jorge, D.J. Martin, M.T.S. Dhanoa, A.S. Rahman, N. Makwana, J.W. Tang, A. Sella, F. Corà, S. Firth, J.A. Darr, P.F. McMillan, H₂ and O₂ evolution from water half-splitting reactions by graphitic carbon nitride materials, *J. Phys. Chem. C* 117 (2013) 7178–7185.
- [59] J.J. Walsh, C. Jiang, J. Tang, A.J. Cowan, Photochemical CO₂ reduction using structurally controlled g-C₃N₄, *Phys. Chem. Chem. Phys.* 18 (2016) 24825–24829.
- [60] H. Hattori, Heterogeneous basic catalysis, *Chem. Rev.* 95 (1995) 537–558.
- [61] H. Park, J.H. Lee, E.H. Kim, K.Y. Kim, Y.H. Choi, D.H. Youn, J.S. Lee, A highly active and stable palladium catalyst on a g-C₃N₄ support for direct formic acid synthesis under neutral conditions, *Chem. Commun.* 52 (2016) 14302–14305.
- [62] S.Q. Song, C.H. Lu, X. Wu, S.J. Jiang, C.Z. Sun, Z.G. Le, Strong base g-C₃N₄ with perfect structure for photocatalytically eliminating formaldehyde under visible-light irradiation, *Appl. Catal. B* 227 (2018) 145–152.
- [63] J.J. Tian, L.X. Zhang, X.Q. Fan, Y.J. Zhou, M. Wang, R.L. Cheng, M.L. Li, X.T. Kan, X.X. Jin, Z.H. Liu, Y.F. Gao, J.L. Shi, A post-grafting strategy to modify g-C₃N₄ with aromatic heterocycles for enhanced photocatalytic activity, *J. Mater. Chem. A* 4 (2016) 13814–13821.
- [64] J.R. Wei, W.L. Shen, J. Zhao, C.W. Zhang, Y.H. Zhou, H.Y. Liu, Boron doped g-C₃N₄ as an effective metal-free solid base catalyst in Knoevenagel condensation, *Catal. Today* 316 (2018) 199–205.
- [65] D. Li, N. Ichikuni, S. Shimazu, T. Uematsu, Catalytic properties of sprayed Ru/Al₂O₃ and promoter effects of alkali metals in CO₂ hydrogenation, *Appl. Catal. A Gen.* 172 (1998) 351–358.
- [66] A. Thomas, A. Fischer, F. Goettmann, M. Antonietti, J.O. Muller, R. Schlögl, J.M. Carlsson, Graphitic carbon nitride materials: variation of structure and morphology and their use as metal-free catalysts, *J. Mater. Chem.* 18 (2008) 4893–4908.
- [67] A.V. Krukau, O.A. Vydrov, A.F. Izmaylov, G.E. Scuseria, Influence of the exchange screening parameter on the performance of screened hybrid functionals, *J. Chem. Phys.* 125 (2006) 224106.
- [68] J. Heyd, G.E. Scuseria, M. Ernzerhof, Hybrid functionals based on a screened Coulomb potential, *J. Chem. Phys.* 118 (2003) 8207–8215.
- [69] B.C. Zhu, L.Y. Zhang, B. Cheng, J.G. Yu, First-principle calculation study of tri-triazine-based g-C₃N₄: a review, *Appl. Catal. B* 224 (2018) 983–999.
- [70] T. Tong, B.C. Zhu, C.J. Jiang, B. Cheng, J.G. Yu, Mechanistic insight into the enhanced photocatalytic activity of single-atom Pt, Pd or Au-embedded g-C₃N₄, *Appl. Surf. Sci.* 433 (2018) 1175–1183.
- [71] M.F. Genisel, M.N. Uddin, Z. Say, M. Kulakci, R. Turan, O. Gulseren, E. Bengu, Bias in bonding behavior among boron, carbon, and nitrogen atoms in ion implanted a-BN, a-BC, and diamond like carbon films, *J. Appl. Phys.* 110 (2011).
- [72] D. Maiti, Y.A. Daza, M.M. Yung, J.N. Kuhn, V.R. Bhethanabotla, Oxygen vacancy formation characteristics in the bulk and across different surface terminations of La_(1-x)Sr_xFe_(1-y)Co_yO_(3-δ) perovskite oxides for CO₂ conversion, *J. Mater. Chem. A* 4 (2016) 5137–5148.
- [73] G. Henkelman, A. Arnaldsson, H. Jonsson, A fast and robust algorithm for Bader decomposition of charge density, *Comput. Mater. Sci.* 36 (2006) 354–360.
- [74] S. Fukuzumi, H. Kotani, K. Ohkubo, S. Ogo, N.V. Tkachenko, H. Lemmetyinen, Electron-transfer state of 9-mesityl-10-methylacridinium ion with a much longer lifetime and higher energy than that of the natural photosynthetic reaction center, *J. Am. Chem. Soc.* 126 (2004) 1600–1601.
- [75] C.Y. Liu, H.W. Huang, W. Cui, F. Dong, Y.H. Zhang, Band structure engineering and efficient charge transport in oxygen substituted g-C₃N₄ for superior photocatalytic hydrogen evolution, *Appl. Catal. B* 230 (2018) 115–124.
- [76] B. Zhu, L. Zhang, D. Xu, B. Cheng, J. Yu, Adsorption investigation of CO₂ on g-C₃N₄ surface by DFT calculation, *J. Co2 Util.* 21 (2017) 327–335.
- [77] Y.J. Ji, H.L. Dong, H.P. Lin, L.L. Zhang, T.J. Hou, Y.Y. Li, Heptazine-based graphitic carbon nitride as an effective hydrogen purification membrane, *RSC Adv.* 6 (2016) 52377–52383.
- [78] L.M. Azofra, D.R. MacFarlane, C. Sun, A DFT study of planar vs. Corrugated graphene-like carbon nitride (g-C₃N₄) and its role in the catalytic performance of CO₂ conversion, *Phys. Chem. Chem. Phys.* 18 (2016) 18507–18514.
- [79] X. Wei, Y. Qiu, W. Duan, Z. Liu, Cathodic and anodic photocurrents generation from melem and its derivatives, *RSC Adv.* 5 (2015) 26675–26679.
- [80] M.K. Marchewka, Infrared and Raman spectra of melaminium chloride hemihydrate, *Mater. Sci. Eng. B-Solid* 95 (2002) 214–221.
- [81] W. Ho, Z. Zhang, M. Xu, X. Zhang, X. Wang, Y. Huang, Enhanced visible-light-driven photocatalytic removal of NO: effect on layer distortion on g-C₃N₄ by H₂ heating, *Appl. Catal. B* 179 (2015) 106–112.
- [82] S.W. Cao, Y. Li, B.C. Zhu, M. Jaroniec, J.G. Yu, Facet effect of Pd cocatalyst on photocatalytic CO₂ reduction over g-C₃N₄, *J. Catal.* 349 (2017) 208–217.
- [83] T.M. Di, B.C. Zhu, B. Cheng, J.G. Yu, J.S. Xu, A direct Z-scheme g-C₃N₄/SnS₂ photocatalyst with superior visible-light CO₂ reduction performance, *J. Catal.* 352 (2017) 532–541.
- [84] Q. Liu, A. Mace, Z. Bacsik, J. Sun, A. Laaksonen, N. Hedin, NaKA sorbents with high CO₂-over-N₂ selectivity and high capacity to adsorb CO₂, *Chem. Commun.* 46 (2010) 4502–4504.
- [85] L. Schwertmann, A. Grunert, A. Pougin, C.H. Sun, M. Wark, R. Marschall, Understanding the influence of lattice composition on the photocatalytic activity of defect-pyrene-structured semiconductor mixed oxides, *Adv. Funct. Mater.* 25 (2015) 905–912.
- [86] S.W. Liu, F. Chen, S.T. Li, X.X. Peng, Y. Xiong, Enhanced photocatalytic conversion of greenhouse gas CO₂ into solar fuels over g-C₃N₄ nanotubes with decorated transparent ZIF-8 nanoclusters, *Appl. Catal. B* 211 (2017) 1–10.
- [87] C. Ricca, A. Grishin, A. Ringuedé, M. Cassir, C. Adamo, F. Labat, Modeling composite electrolytes for low-temperature solid oxide fuel cell application: structural, vibrational and electronic features of carbonate–oxide interfaces, *J. Mater. Chem. A* 4 (2016) 17473–17482.
- [88] Y. Dai, X.P. Wu, Y. Tang, Y. Yang, X.Q. Gong, J. Fan, Selectivity switching resulting in the formation of benzene by surface carbonates on ceria in catalytic gas-phase oxidation of benzyl alcohol, *Chem. Commun.* 52 (2016) 2827–2830.
- [89] W.C. Wilfong, C.S. Srikanth, S.S. Chuang, In situ ATR and DRIFTS studies of the nature of adsorbed CO₂ on tetraethylenepentamine films, *ACS Appl. Mater. Interfaces* 6 (2014) 13617–13626.
- [90] L.J. Liu, H.L. Zhao, J.M. Andino, Y. Li, Photocatalytic CO₂ reduction with H₂O on TiO₂ nanocrystals: comparison of anatase, rutile, and brookite polymorphs and exploration of surface chemistry, *ACS Catal.* 2 (2012) 1817–1828.
- [91] G.H. Yin, X.Y. Huang, T.Y. Chen, W. Zhao, Q.Y. Bi, J. Xu, Y.F. Han, F.Q. Huang, Hydrogenated blue titania for efficient solar to chemical conversions: preparation, characterization, and reaction mechanism of CO₂ reduction, *ACS Catal.* 8 (2018) 1009–1017.
- [92] S. Enthaler, J. von Langermann, T. Schmidt, Carbon dioxide and formic acid—the couple for environmental-friendly hydrogen storage? *Energy Environ. Sci.* 3 (2010) 1207–1217.
- [93] X. Wang, Q. Meng, L. Gao, Z. Jin, J. Ge, C. Liu, W. Xing, Recent progress in hydrogen production from formic acid decomposition, *Int. J. Hydrogen Energy* 43 (2018) 7055–7071.
- [94] M. Anpo, H. Yamashita, Y. Ichihashi, S. Ehara, Photocatalytic reduction of CO₂ with H₂O on various titanium oxide catalysts, *J. Electroanal. Chem.* 396 (1995) 21–26.
- [95] S.S. Tan, L. Zou, E. Hu, Kinetic modelling for photosynthesis of hydrogen and methane through catalytic reduction of carbon dioxide with water vapour, *Catal. Today* 131 (2008) 125–129.
- [96] P. Giannozzi, S. Baroni, N. Bonini, M. Calandra, R. Car, C. Cavazzoni, D. Ceresoli, G.L. Chiarotti, M. Cococcioni, I. Dabo, A. Dal Corso, S. de Gironcoli, S. Fabris, G. Fratesi, R. Gebauer, U. Gerstmann, C. Gougousis, A. Kokalj, M. Lazzeri, L. Martin-Samos, N. Marzari, F. Mauri, R. Mazzarello, S. Paolini, A. Pasquarello, L. Paulatto, C. Sbraccia, S. Scandolo, G. Sclauzero, A.P. Seitsonen, A. Smogunov, P. Umari, R.M. Wentzcovitch, QUANTUM ESPRESSO: a modular and open-source software project for quantum simulations of materials, *J. Phys. Condens. Matter* 21 (2009) 39502.
- [97] P. Giannozzi, O. Andreussi, T. Brumme, O. Bunau, M. Buongiorno Nardelli, M. Calandra, R. Car, C. Cavazzoni, D. Ceresoli, M. Cococcioni, N. Colonna, I. Carnimeo, A. Dal Corso, S. de Gironcoli, P. Delugas, R.A. DiStasio, A. Ferretti, A. Floris, G. Fratesi, G. Fugallo, R. Gebauer, U. Gerstmann, F. Giustino, T. Gorni,

- J. Jia, M. Kawamura, H.Y. Ko, A. Kokalj, E. Kucukbenli, M. Lazzeri, M. Marsili, N. Marzari, F. Mauri, N.L. Nguyen, H.V. Nguyen, A. Otero-de-la-Roza, L. Paulatto, S. Ponce, D. Rocca, R. Sabatini, B. Santra, M. Schlipf, A.P. Seitsonen, A. Smogunov, I. Timrov, T. Thonhauser, P. Umari, N. Vast, X. Wu, S. Baroni, Advanced capabilities for materials modelling with Quantum ESPRESSO, *J. Phys. Condens. Matter* 29 (2017) 465901.
- [98] A. Dal Corso, Pseudopotentials periodic table: from H to Pu, *Comput. Mater. Sci.* 95 (2014) 337–350.
- [99] G. Kresse, D. Joubert, From ultrasoft pseudopotentials to the projector augmented-wave method, *Phys. Rev. B* 59 (1999) 1758–1775.
- [100] P.E. Blochl, Projector augmented-wave method, *Phys. Rev. B* 50 (1994) 17953–17979.
- [101] J.P. Perdew, K. Burke, M. Ernzerhof, Generalized gradient approximation made simple, *Phys. Rev. Lett.* 77 (1996) 3865–3868.
- [102] S. Grimme, J. Antony, S. Ehrlich, H. Krieg, A consistent and accurate ab initio parametrization of density functional dispersion correction (DFT-D) for the 94 elements H-Pu, *J. Chem. Phys.* 132 (2010) 154104.
- [103] K. Momma, F. Izumi, VESTA 3 for three-dimensional visualization of crystal, volumetric and morphology data, *J. Appl. Crystallogr.* 44 (2011) 1272–1276.